Full length article

The fabrication of graphene-reinforced Al-based nanocomposites using high-pressure torsion

Yi Huang [a, b, *], Piotr Bazarnik [c], Diqing Wan [d], Dan Luo [e], Pedro Henrique R. Pereira [f], Malgorzata Lewandowska [c], Jin Yao [g], Brian E. Hayden [g], Terence G. Langdon [b]

[a] Department of Design and Engineering, Faculty of Science and Technology, Bournemouth University, Poole, Dorset, BH12 5BB, UK
[b] Materials Research Group, Department of Mechanical Engineering, University of Southampton, Southampton, SO17 1BJ, UK
[c] Faculty of Materials Science and Engineering, Warsaw University of Technology, Woloska 141, 02-507 Warsaw, Poland
[d] School of Mechanical and Electronical Engineering, East China Jiaotong University, Nanchang, Jiangxi Province, 330013, PR China
[e] LiME BCAST, Brunel University London, Uxbridge, Middlesex, UB8 3PH, UK
[f] Department of Metallurgical and Materials Engineering, Universidade Federal de Minas Gerais, Belo Horizonte, MG 31270-901, Brazil
[g] Advanced Composite Materials Facility, Department of Chemistry, University of Southampton, Southampton, SO17 1BJ, UK

ARTICLE INFO

ABSTRACT

Metal matrix nanocomposites were fabricated by high-pressure torsion (HPT) using 5% graphene nanoplates as a reinforcement contained within an Al matrix. Powders were mixed and compacted at room temperature and then processed by HPT at three different temperatures of 298, 373 and 473 K. After processing, microstructural observations were undertaken to reveal the distributions of graphene in the matrix, the grain refinement in the aluminium and the nature of the graphene-aluminium interfaces. Tests were performed to measure the microhardness, the tensile stress-strain curves and the electrical conductivity. The results show that processing by HPT is advantageous because it avoids the sintering and high temperature deformation associated with other processing routes.
© 2018 Acta Materialia Inc. Published by Elsevier Ltd. This is an open access article under the CC BY-NC-ND license (http://creativecommons.org/licenses/by-nc-nd/4.0/).

1. Introduction

Metal matrix composites (MMCs) are lightweight structural materials having wide applications in the aerospace, automotive and electronic sectors [1]. Boron, carbon and silicon carbide (SiC) are often used as continuous fibre reinforcements and silicon carbide (SiC_p), alumina (Al_2O_3) and boron carbide (B_4C) are conventional particle reinforcements [2]. Aluminium-based MMCs have attracted much interest due to the strengthening effects from different reinforcements such as Al_2O_3 and SiC [3]. An alternative reinforcement is graphene which was discovered in the last 15 years [4] and has a low mass density of $0.77\,mg\,m^{-2}$ [5], outstanding mechanical properties with a 1 TPa Young's modulus and 130 GPa tensile strength [6], as well as high thermal conductivity above $4000\,W\,mK^{-1}$ [7] and high electronic conductivity above $15000\,cm\,V^{-2}$ [8]. The 2D geometry of graphene nanosheets and nanoplates is responsible for producing maximum values for their surface-to-volume ratios so that graphene appears as an ideal candidate for incorporation in an aluminium matrix to achieve high strength and conductivity. Graphene nanoplates (GNPs), which consist of multilayer graphene, are much cheaper and easier to produce than single layer graphene [9] but the high van der Waals forces between the graphene layers tends to limit the uniform dispersion of GNPs within the metal matrix.

The traditional fabrication routes for MMCs can be divided into liquid state (liquid metal infiltration and casting techniques) and solid state (powder metallurgy) methods [10]. Liquid metal infiltration and casting involves an incorporation of a dispersed particulate into a molten matrix metal, followed by its solidification. However, due to the large density difference between graphene and the metal matrix, it is difficult to disperse graphene uniformly within the matrix and the liquid processing methods usually produce agglomerated particles in the ductile matrix which lead to an unwanted brittle nature. Furthermore, the agglomeration is more severe when the particulate size is in the submicrometer or

---

* Corresponding author. Department of Design and Engineering, Faculty of Science and Technology, Bournemouth University, Poole, Dorset, BH12 5BB, UK.
E-mail address: yhuang2@bournemouth.ac.uk (Y. Huang).

nanoscale range [11] which is the case when using graphene as the reinforcement. The alternative of powder metallurgy (PM) processing techniques generally involve sintering, cold isostatic pressing, hot isostatic pressing or spark plasma sintering, and in some cases secondary deformation such as hot extrusion, hot forging, hot rolling and/or friction stir processing. The PM processing has two major disadvantages. The first disadvantage is an oxidation of the metal matrix and the production of unclean interfaces between the particulates and the matrix which lead to a weak bonding and consequent low mechanical strength [12]. In addition, processing at elevated temperatures aids the chemical reactions between the matrix and particles which may produce brittle secondary phases [13]. The second disadvantage is that high temperature sintering can produce unexpected grain growth in the matrix [14]. Nevertheless, it is generally easier to achieve uniformity of the reinforcement distributions using PM processing rather than liquid processing [15].

Several recent reports have described the synthesis of graphene-reinforced Al matrix composites [16—28] including using a liquid method [16], ball milling plus hot isostatic pressing, hot pressing or hot extrusion [17—21], ball milling plus sintering [22], sintering or sintering plus extrusion [23—25], spark plasma sintering [26,27] or an ultrasonic treatment plus friction stir processing [28]. In practice, these various investigations all involve high temperature processing steps which may cause oxidation of the metal matrix and/or reactions between the graphene and the matrix. Thermodynamic calculations show that the Al and graphite may react to form Al_4C_3 at high temperature [29]. Therefore, in order to overcome these technical challenges, it is important to consider developing the composites using a low temperature approach. One possibility is to use high-pressure torsion (HPT) which is a severe plastic deformation technique that introduces significant grain refinement and corresponding strength enhancement in bulk metals in particular when processing at relatively low temperatures [30,31]. Currently, there are reports on the HPT processing of powder materials such as pure metals [32—36], composites reinforced with Al_2O_3 and SiC particulates [37—40] and composites reinforced with carbon-based particles such as fullerenes (C_{60}) and carbon nanotubes (CNTs) [41—48]. These MMCs can be effectively processed by HPT at temperatures between 298 and 473 K and this range is much lower than the typical sintering temperatures of 863—893 K for Al alloys. Furthermore, the use of low temperature HPT processing will avoid oxidation and the formation of second phases. There is also mass transfer within the samples due to the development of turbulent eddy currents in the sample cross-sections during HPT processing, as confirmed by computer modelling [49] and experimental observations in immiscible alloys [50,51], and this will help in the redistribution of reinforcements within the metal matrix. In addition, there are currently no reports on using HPT to fabricate graphene-reinforced Al-based MMCs (henceforth designated graphene-Al composites).

The present research was therefore initiated in order to evaluate the use of HPT processing in the fabrication of graphene-Al composites at temperatures ranging from 298 to 473 K, to develop a comprehensive understanding of the microstructural developments in both the Al matrix and the graphene, and to measure experimentally the strength and conductivity in the fabricated composites.

2. Experimental materials and procedures

Aluminium powder with a mean particle size of 125 μm was purchased from Goodfellow (Cambridge, UK). The purity of the powder, as provided by the supplier, was 99.5% with Cu < 200, Fe < 3500, Mn < 200, and Si < 2500 ppm; this composition is similar to the specifications for commercial purity Al-1050 aluminium in ASTM B491. Graphene nanoplates (GNPs) were purchased from Sigma-Aldrich (Gillingham, Dorset, UK) with Raman D/G (the ratio of D band peak to G band peak) and D/D′ (the ratio of D band peak to D′ band peak) values of 0.28 and 5.0, respectively. The 2D band shape indicates the presence of graphene flakes of a few layers with an average of ~5—7 atomic layers. Fig. 1(a) shows the scanning electron microscope (SEM) images of the as-received GNPs and the higher magnification image in Fig. 1(b) shows an agglomeration of GNPs.

The aluminium powder was initially mixed with 5% of GNPs in weight percentage and the mixed powders were then poured into a glass bottle and rotated on a rotation rack for 30 min to improve the homogeneity of GNPs in the Al powder. The mixed powders were
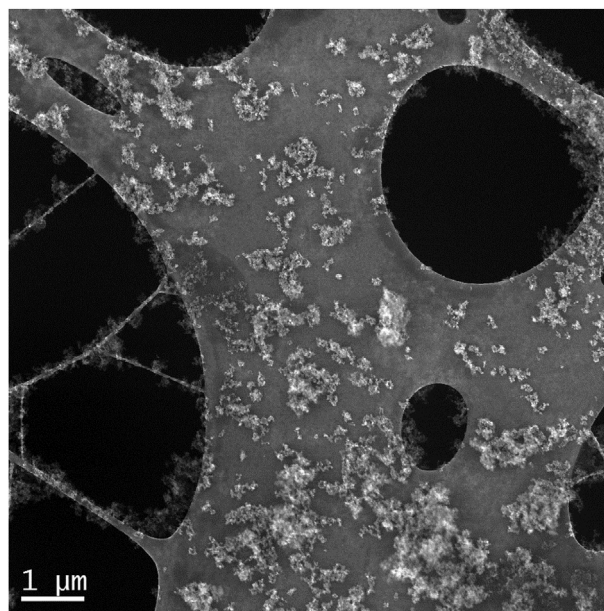
(a)
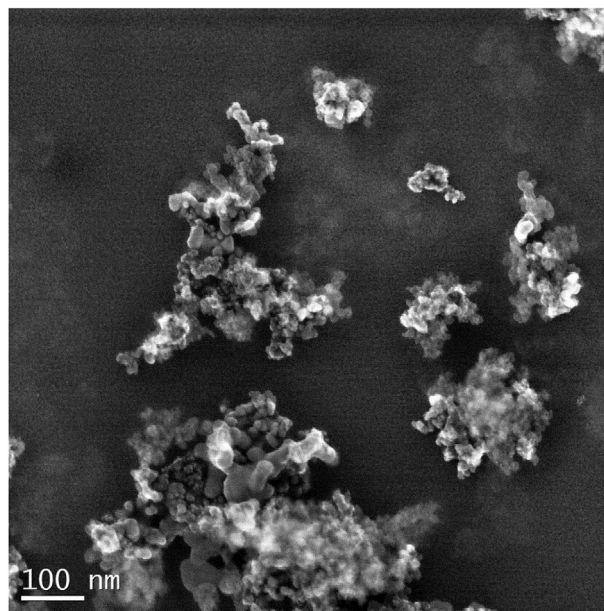
(b)

Fig. 1. SEM images of as-received GNPs powder at (a) low and (b) high magnifications.

compacted in a die at room temperature under a pressure ~40 MPa for 1 min to provide disc-shaped tablets with diameters of 10 mm and heights of ~1.2 mm.

The HPT processing was conducted at temperatures of 298, 373 and 473 K under quasi-constrained conditions where there is a small outflow of material around the periphery of the disc during processing [52]. At each temperature, the pre-compacted disc-shaped tablets were initially subjected to a pressure of 6.0 GPa for 1 min without any shear deformation where this processing condition is henceforth designated 0 turns. Thereafter, the samples were processed by torsional straining through numbers of rotations, *N*, of 1, 5, 10 and 20 turns.

After processing, each disc was cut into two halves along a diameter using a diamond wafering saw. The cross-sections of each disc were examined using SEM with the specimens prepared by grinding and ion polishing using an Hitachi Ion Milling System IM-4000. Since ion milling is a damageless process, this polishing eliminates all deformation and oxide layers and the surface quality was sufficiently good that the structure was examined by SEM using channelling contrast. Microstructure examinations were conducted using an Hitachi SU-8000 SEM operating at 10 kV. The images were taken in secondary electron (SE) imaging and in back-scattered electron (BSE) modes. The SEM observations were performed on cross-section planes in the middle region close to the disc centre and in the edge region at ~0.5 mm from the disc edge. Detailed microstructural observations from selected areas were recorded using a Cs-corrected dedicated high resolution scanning transmission electron microscope (STEM) Hitachi HD-2700 operating at an accelerating voltage of 200 kV. The STEM thin foils were extracted from the peripheral parts of each disc using a focused ion beam (FIB) Hitachi NB 5000 microscope. The STEM observations were taken in bright-field (BF) and high-angle annular dark field (HAADF or Z-contrast) modes. The grain size of the HPT-processed Al matrix was measured using the linear intercept method with Image J software based on the SEM and STEM images.

XploRA confocal Raman spectroscopy was used to examine the structure change of the graphene during HPT processing. The Raman spectra were acquired with a selected laser wavelength of 532 nm at room temperature.

The mechanical properties of HPT-processed samples were evaluated using microhardness measurements and tensile testing. The Vickers microhardness, Hv, was measured along radial directions on the polished disc surfaces using an FM-300 micro-hardness tester with a load of 200 g (equivalent to 1.96 N) and a dwell time of 15 s. Miniature tensile specimens having gauge lengths of 1.1 mm, widths of 0.95 mm and thicknesses of ~0.7 mm were cut from the HPT-processed discs. These specimens were tested in tension at 298 K using a Zwick 30 kN Proline facility operating at a constant rate of cross-head displacement with an initial strain rate of $1.0 \times 10^{-3} \text{ s}^{-1}$. The constant cross-head velocity testing machine applies a constant strain rate that is the sum of the elastic and plastic strain rates in the specimen and the strain rate resulting from the elasticity of the testing machine [53]. The load and displacement data were converted to engineering stress and engineering strain using the method described elsewhere [54] where the influence of the elastic deformation of the testing apparatus was minimised by equating the elastic portion of the stress-strain curves to the theoretical elastic modulus of aluminium. To check on reproducibility, four samples were tested for each condition.
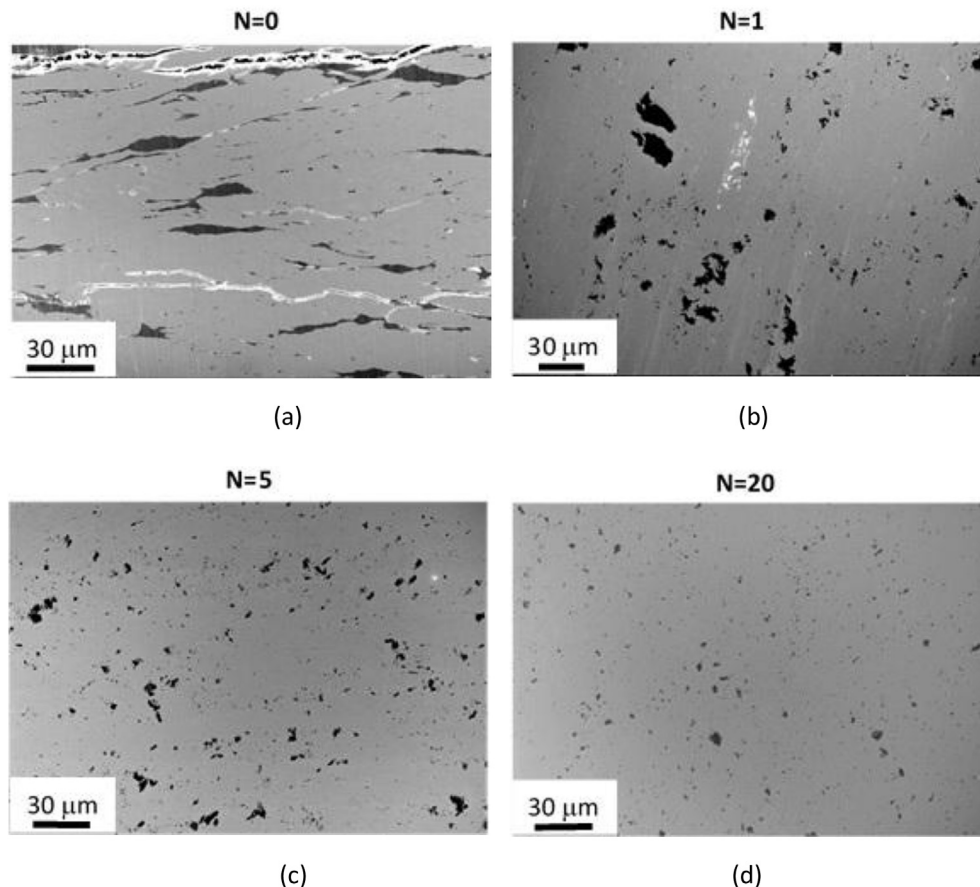

Fig. 2. The distribution of 5% GNPs in the Al matrix processed by HPT at 298 K with (a) $N = 0$, (b) $N = 1$, (c) $N = 5$ and (d) $N = 20$.

The bulk electrical resistivity (ohms-cm) of HPT-processed disc samples was measured on a 4D automatic four-points probe meter (Model 280) using a linear probe with a probe size of 500 μm and a probe-to-probe distance of 1 mm. For each disc sample, the bulk electrical resistivity was measured at 5 or more positions within the disc half-radius area. The measured bulk resistivity (ohms-cm) was compared with the bulk resistivity of annealed commercial pure Cu ($1.72 \times 10^{-6}\,\Omega$-cm), and then it was converted to the electrical conductivity represented by the IACS (International Annealed Copper Standard) using the expression IACS (%) $= 1.72 \times 10^{-6}\,\Omega$-cm/(the measured bulk electrical resistivity in ohm-cm) [55].

3. Experimental results

3.1. The evolution of the GNPs distributions in the Al matrix during HPT processing

The polished cross-sectional surfaces of samples processed by HPT at 298 K were observed by SEM and the SE images giving the GNPs distributions in the Al matrix are shown in Fig. 2 after 0, 1, 5 and 20 turns, where the GNPs have a black colour in these images. In the sample compressed under 6.0 GPa for 1 min (0 turns sample), large cracks with shining reflections appear at the upper and lower regions of the disc in Fig. 2(a) and the GNPs are in the form of agglomerates displaying flow tendencies. By contrast, no cracks are visible in samples processed to 1, 5 and 20 turns in Fig. 2(b–d). Furthermore, with increasing numbers of turns there is less evidence for a flow tendency in the agglomerated GNPs, and the size of the agglomerates is reduced significantly as *N* increases from 5 to

20 turns.

Similar polished cross-sectional surfaces were examined after HPT at 473 K and the results are shown in Fig. 3(a–d). No large cracks are visible in the 0 turns sample in Fig. 3(a) although there are some very short cracks in the top area of the SE image but the agglomerated GNPs have no obvious flow tendency. Comparing Figs. 3(a) and 2(a), it is apparent that HPT processing at 473 K promotes diffusion and plastic flow which reduces the cracking in the 0 turns sample. The agglomeration of GNPs in the Al matrix also changes with increasing numbers of turns as shown in Fig. 3(b–d) such that the agglomerated GNPs are fragmented to much smaller sizes after 5 and 20 turns by comparison with the samples processed at 298 K. This shows that the shear deformation induced by HPT processing is effective in reducing cracking and in prompting the material flow and the fragmentation of the agglomerates of GNPs in the Al matrix.

3.2. Microstructure development in the Al matrix during HPT processing

The polished surfaces of the 0 turns samples processed by HPT at 298 and 473 K were further observed by SEM at higher magnifications to reveal the grain structure in the Al matrix and the occurrence of local bonding between the GNPs and the Al matrix. Fig. 4(a) and (b) show the same area observed by the SE and BSE mode for the 0 turns sample processed at 298 K. The SE image in Fig. 4(a) demonstrates that most of the agglomerated GNPs have good bonding with the metal matrix and some of them have comet-tails which confirm the strong flow tendency after compression at 6.0 GPa for 1 min. Some cracks formed around the GNPs and also
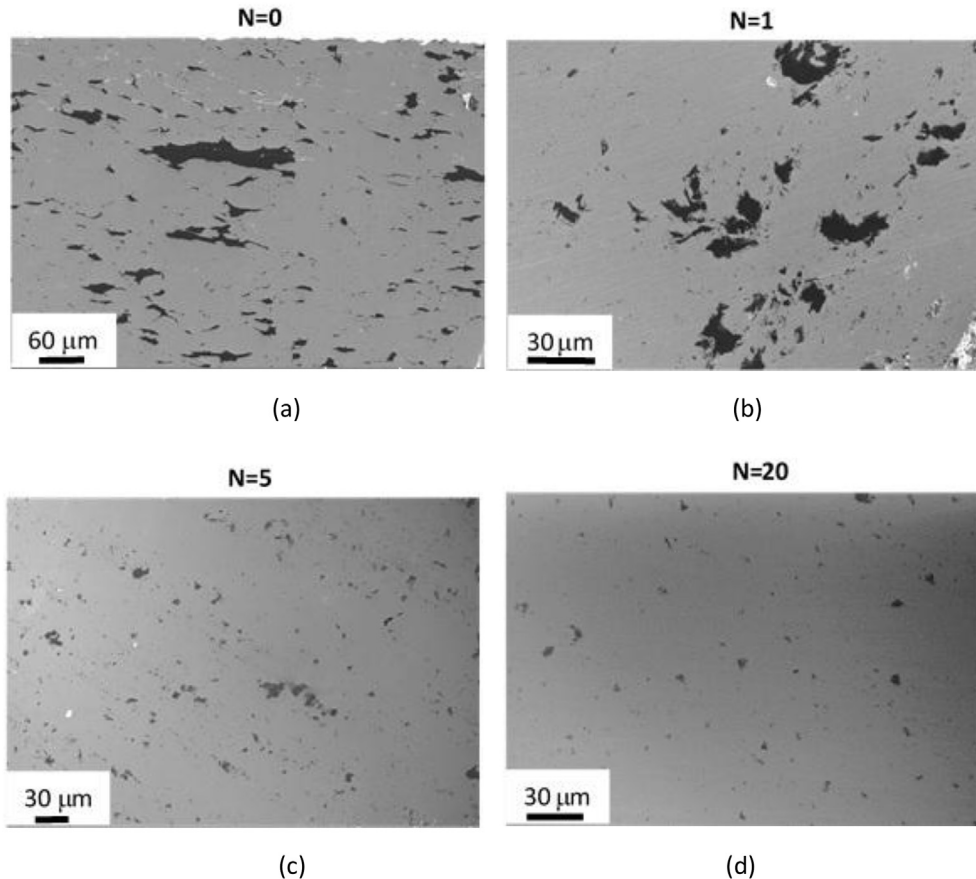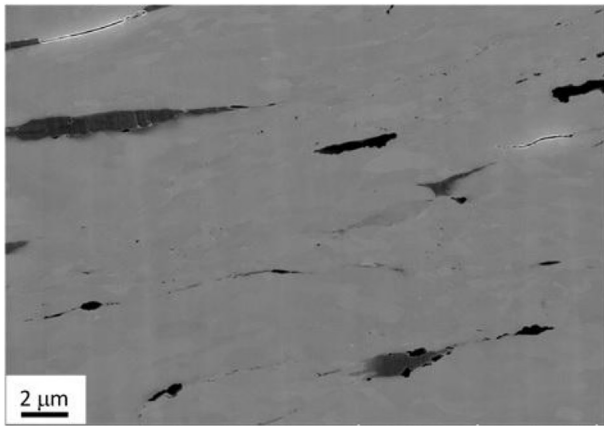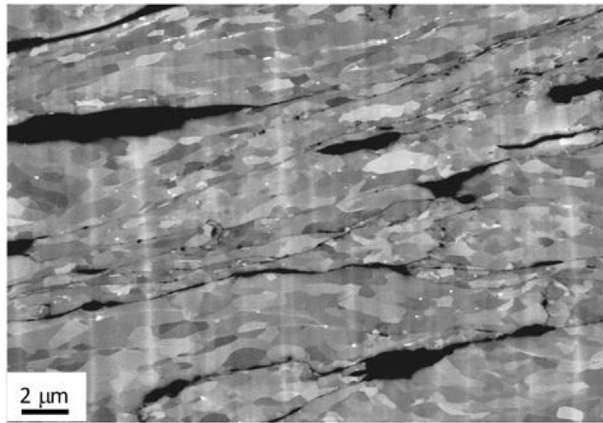

Fig. 3. The distribution of 5% GNPs in the Al matrix processed by HPT at 473 K with (a) $N=0$, (b) $N=1$, (c) $N=5$ and (d) $N=20$.
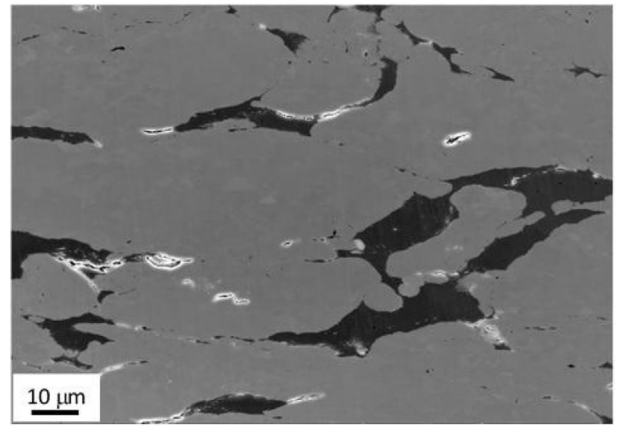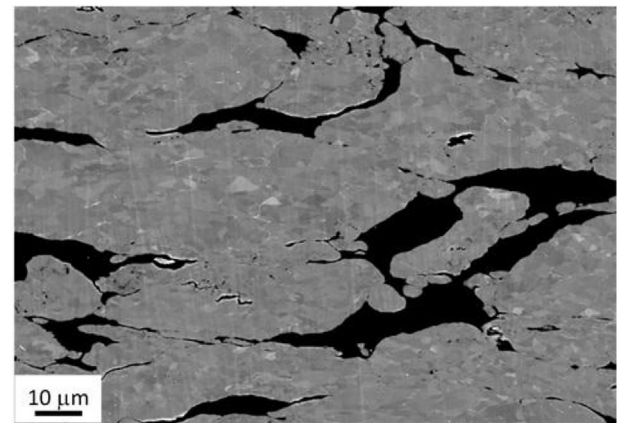
(a)

(b)

Fig. 4. Microstructures of 0 turns sample processed by HPT at 298 K: same area observed using different SEM modes of (a) secondary electron image and (b) back scattered image.

(a)

(b)

Fig. 5. Microstructures of 0 turns sample processed by HPT at 473 K: same area observed using different SEM modes of (a) secondary electron image and (b) back scattered image.

some isolated cracks formed within the Al matrix. The BSE image in Fig. 4(b) reveals the grain structure and the white regions of lines or dots were identified by EDX analysis as Fe-Si rich phases which is consistent with the compositional analysis of the Al powder. When the compact tablet is subjected only to compression as at 0 turns, the axial compression gives a radial flow tendency so that most of the grain structure tends to be elongated with a measured average grain size of ~0.5 μm along the shorter axes of the grains. It is important to note that the cracks and GNPs both appear as a black colour in the BSE image in Fig. 4(b) so that the cracks and GNPs can be identified only in the SE image in Fig. 4(a). Similar observations were recorded for the 0 turns sample processed by HPT at 473 K in Fig. 5 where the GNPs have no obvious flow tendency and there is a network-like bonding with the Al matrix. It is evident from Fig. 5(b) that the grains are reasonably equiaxed in structure with an average grain size of ~1.5 μm.

Fig. 6 shows the STEM images of samples processed to (a) 1, (b) 5 and (c) 20 turns of HPT at 298 K: each row shows two images where the left column is a high resolution STEM image so that the GNPs appear white and the right column is a HAADF image (or Z-contrast image) of the same area where the GNPs are black based on the compositional difference. Normally, heavy elements are brighter in Z-contrast images and, since the carbon atoms in graphene are lighter than the aluminium atoms, the graphene appears dark in the Z-contrast images. For convenience, the observable GNPs are marked with white arrows in both the STEM and Z-contrast images.

By comparing the two sets of images for each sample, it is apparent that the presence of GNPs is resolved more clearly in the Z-contrast images. No cracks or voids exist between the GNPs and the Al matrix after processing to 1, 5 and 20 turns but with increasing through 1, 5 and 20 turns at 298 K the average grain size of the Al matrix is reduced through ~180, ~90 and ~70 nm, respectively. Fig. 7 shows comparable images after processing at 473 K for (a) 1, (b) 5 and (c) 20 turns: as in Fig. 6, the observable GNPs are marked with white arrows. Thus, the GNPs show good bonding with the Al matrix without the detection of any cracks or voids. The average grain sizes after 1, 5 and 20 turns at 473 K were ~700, ~295 and ~155 nm, respectively, and these values are larger than at 298 K.

3.3. The nature of the interfaces between the GNPs and the Al matrix during HPT processing

Samples processed by HPT at 298 and 473 K were observed under high resolution STEM to reveal the bonding interface and the surface features of the GNPs: representative STEM images are presented in Figs. 8 and 9.

Fig. 8 shows STEM images of 1 turn samples processed by HPT at 298 K. Thus, when the graphene (0001) nanoplates have a different orientation from the (111) crystal plane of the Al matrix, there is an interface transition zone in which the C and Al atoms accommodate
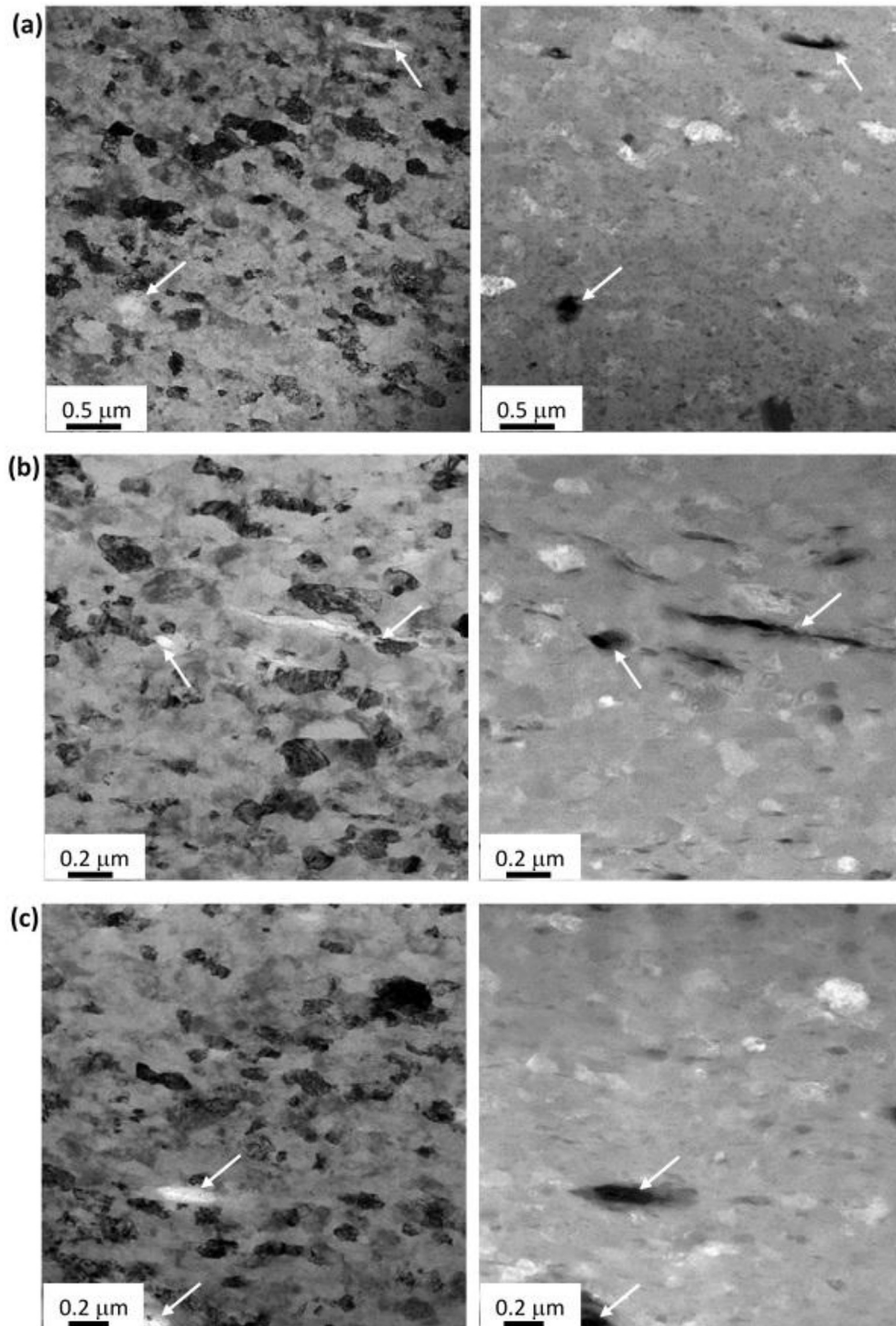
Fig. 6. STEM and Z-contrast images showing the microstructures of samples processed by HPT at 298 K for (a) $N = 1$, (b) $N = 5$ and (c) $N = 20$.

each other as shown in Fig. 8(a). The measured layer-to-layer distance of the GNPs is ~0.35 nm in Fig. 8(a) which is similar to the layer-to-layer distance reported for carbon nanotubes [48] whereas the Al (111) interplanar spacing is ~0.23 nm. The GNPs show a long intact layered structure and there are only slight bends as indicated by white arrows in Fig. 8(b). These results are reasonable because of the small amounts of shear strain applied to the graphene-Al composite in 1 turn of HPT processing.

Comparable STEM images are shown in Fig. 9 for 5 turns

samples processed by HPT at 473 K. Thus, the GNPs exist not only in the grain boundary area in Fig. 9(a) but also within the Al matrix in Fig. 9(b) as highlighted by white arrows. The GNPs embedded within these ultrafine grains are critical for achieving a significant strength enhancement in the graphene-Al composites. Based on these observations of samples processed by HPT at 298 and 473 K, it is concluded that the GNPs display more bending as the numbers of turns increase and this is consistent with the high levels of internal stress introduced by the heavy shear deformation.
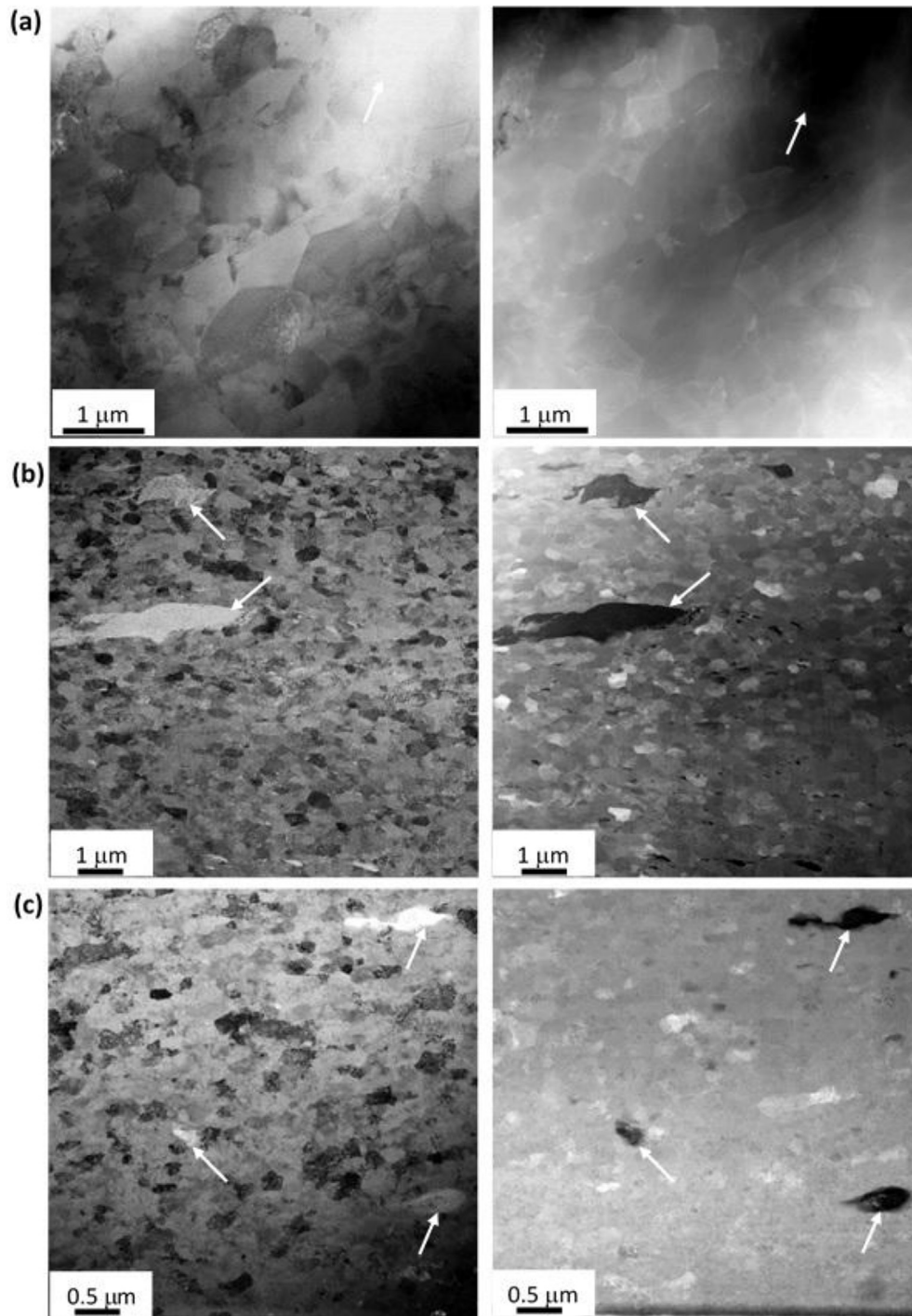
Fig. 7. STEM and Z-contrast images showing the microstructures of samples processed by HPT at 473 K for (a) $N = 1$, (b) $N = 5$ and (c) $N = 20$.

Raman spectroscopy is a convenient and effective method for characterizing carbon materials and Fig. 10 shows the Raman spectra of GNPs in the 20 turns sample processed by HPT at 298 K. The characteristic peaks of the disorder-induced D band ($\sim$1353 cm^{-1}) and G band (1580 cm^{-1}) were detected, where the D band is associated with non-sp^2 disorders (sp^3-hybridized carbon) which are present in the network of sp^2-hybridized carbon, whereas the G band is a typical ordered graphite structure that is attributed to the degree of crystallinity of sp^2-bonded carbon materials [56]. The intensity ratio of the D band to G band (I_D/I_G) is a measure of the defects present in the GNPs after HPT processing, where a high ratio

indicates a higher defect density in carbon materials [57]. In Fig. 10, the ratio is $\sim$1.15 indicating that some defects exist in the GNPs after 20 turns, where this is consistent with the observed bends of the GNPs in the STEM images in Figs. 8 and 9.

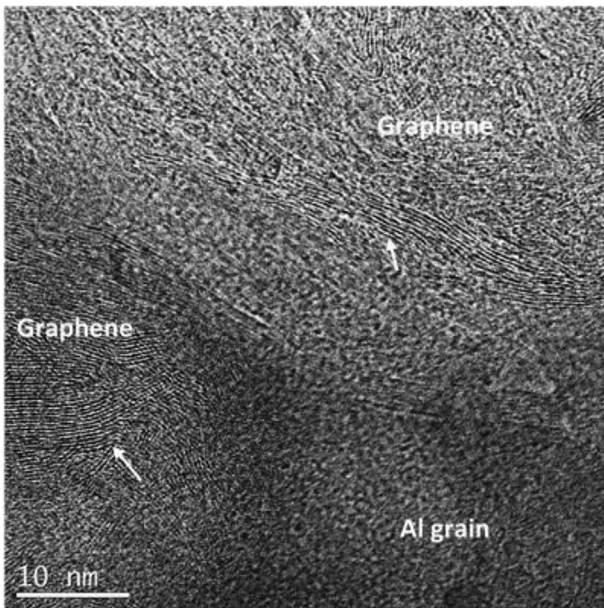### 3.4. Mechanical properties of HPT-processed graphene-Al nanocomposites

Fig. 11 shows the evolution of microhardness in the composites processed by HPT at (a) 298, (b) 373 and (d) 473 K, respectively. At 298 K, there is no large difference in hardness between the 0 turns
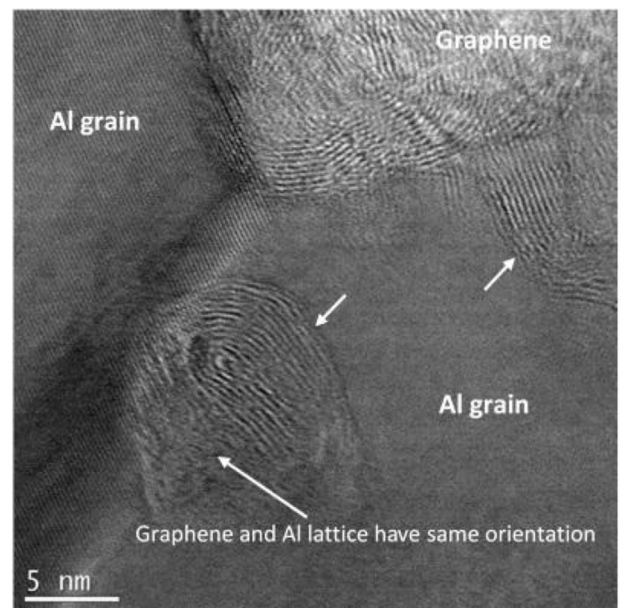
(a)
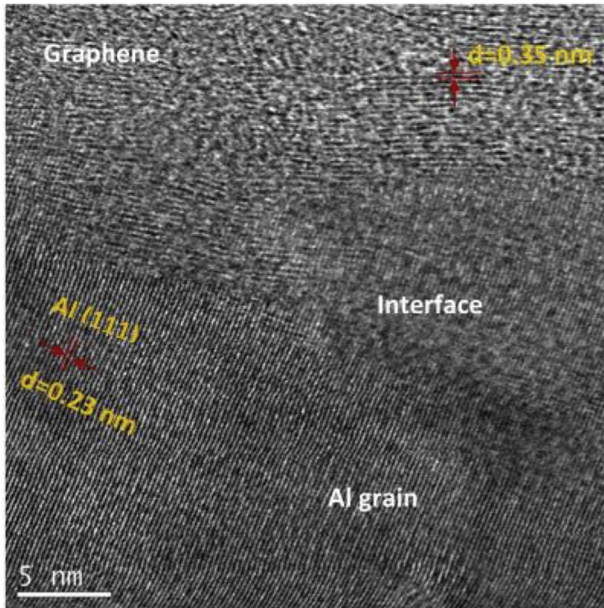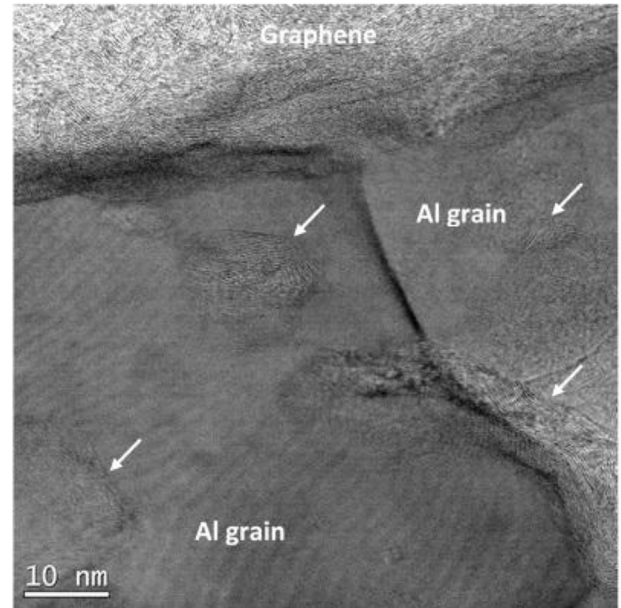
(b)

Fig. 8. High resolution STEM images of 1 turn sample processed by HPT at 298 K showing the interface between GNPs and the Al matrix under the condition of (a) graphene nanoplates and Al matrix having different orientations, (b) the existence of long straight and slightly curved GNPs in the Al matrix.

(a)

(b)

Fig. 9. High resolution STEM images of 5 turns sample processed by HPT at 473 K showing the interface between GNPs and the Al matrix under the condition of (a) the existence of GNPs not only in the grain boundary area but also within the Al matrix, (b) part of the curved graphene nanoplates having the same orientation with Al matrix.

and 1 turn samples in Fig. 11(a) and all values are in the range ~40–60 Hv which shows that 1 turn of HPT introduces no significant deformation in the Al matrix. As the numbers of turns increases to 5 and 10, the hardness distributions show the typical trends observed in most bulk metals with lower hardness values in the disc centre areas and higher hardness values in the disc outer areas [58]. With a further increase in the numbers of turns to 20, the centre area shows only a slight increase in hardness but from the half-radius position to the disc edge the hardness values lie around a plateau with a value of ~110 Hv which confirms that heavy straining introduces a saturation state. At 373 K, hardness

distributions in Fig. 11(b) are similar except there is no well-defined plateau distribution after 20 turns. In Fig. 11(c) for HPT at 473 K the maximum hardness values are ~90 Hv after 20 turns and the hardness values for the samples processed to 10 and 20 turns are almost identical.

Tensile testing was conducted at room temperature with an initial strain rate of $1.0 \times 10^{-3} \text{ s}^{-1}$ on samples processed by 20 turns at three different temperatures. As shown in Fig. 12, the strength of the graphene-Al nanocomposite decreases with increasing processing temperature and the maximum strengths are ~350, ~340 and ~290 MPa after processing at 298, 373 and 473 K, respectively.
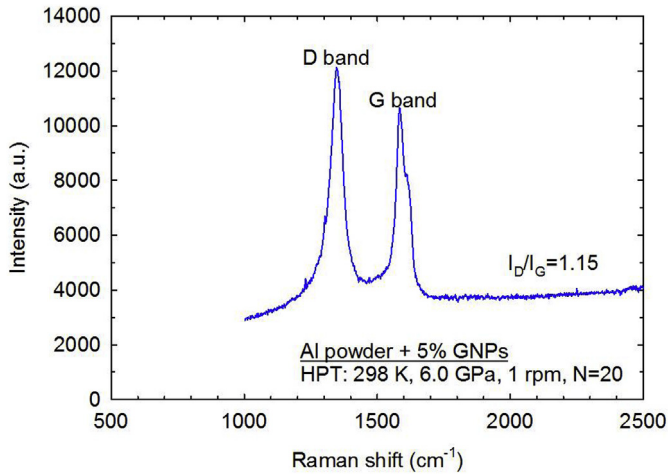
Fig. 10. Raman spectroscopy of GNPs after HPT processing to 20 turns at 298 K.

Inspection shows that the elongations exhibit no simple variation with processing temperature and the measured elongations for these three temperatures are ~1.8%, ~3.9% and ~2.1%, respectively.

3.5. Electrical conductivity of the HPT-processed graphene-Al composites

For comparison purposes, Table 1 shows electrical conductivity measurements in the HPT-processed graphene-Al composite. The electrical conductivity of commercial purity Al is 62% IACS [59]. When graphene-Al composites are processed by HPT at 298 K, the average electrical conductivity in samples taken through 5 and 20 turns are $66.7 \pm 4.0\%$ and $64.9 \pm 2.1\%$ IACS, respectively. Considering the relatively large error bar ranges, the conductivity in the sample with the larger shear deformation is only slightly lower than the sample with the smaller shear deformation. To check whether the HPT processing temperature has an influence, the electrical conductivity was also measured after processing by HPT for 20 turns at 473 K. The result is shown in Table 1 and it confirms there is an increase in conductivity with increasing HPT processing temperature which is consistent with data reported for the processing of a Cu-Cr alloy by HPT [60]. It is also consistent with the result for a Cu-Cr alloy showing that the conductivity is increased when samples are subjected to heat treatments after HPT [61].

4. Discussion

### 4.1. The use of HPT in dispersing agglomerated GNPs within an Al matrix

The generally accepted theory of HPT is based on the assumptions of a uniformity of simple shear deformation through the height of the specimen but with the localized shear strain proportional to the distance from the disc centre [62]. However, several recent investigations show deviations from this simple model. For example, in the HPT processing of a duplex stainless steel there is evidence for the formation of significant local turbulence including the presence of double-swirl patterns and local shear strain vortices [63—67]. Double-swirl flow patterns were reported also in a Cu-28% Ag alloy after HPT processing [68] and there are recent simulations demonstrating that non-laminar or turbulent flow causes intensive mass transfer and a mixing of the deformed material [49,69]. This explains the improved uniformity of particle size distribution in an Al-6061 matrix alloy reinforced with Al_2O_3
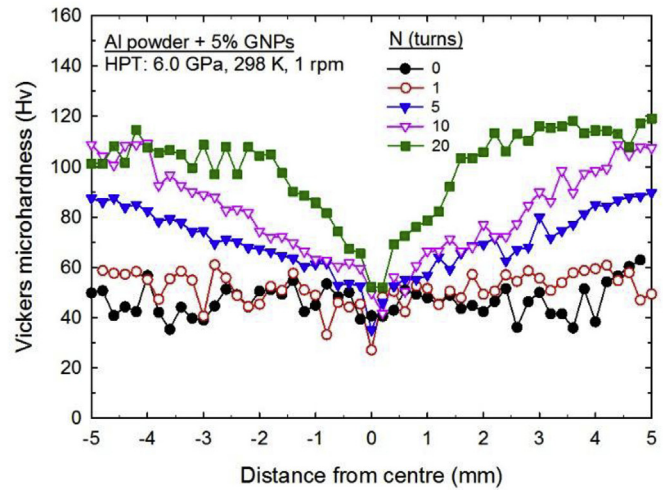
(a)
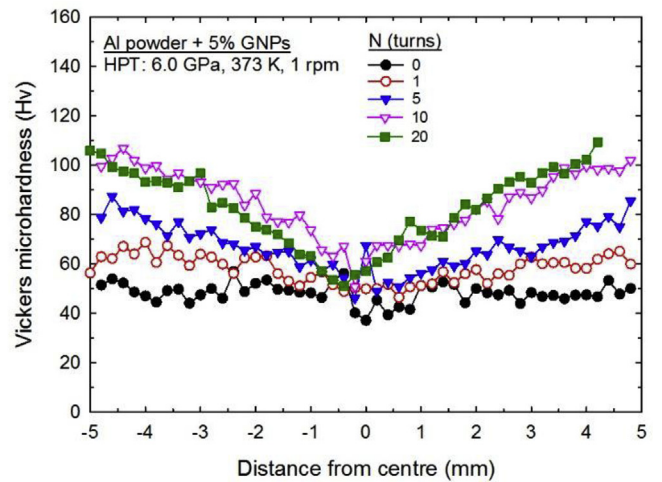
(b)
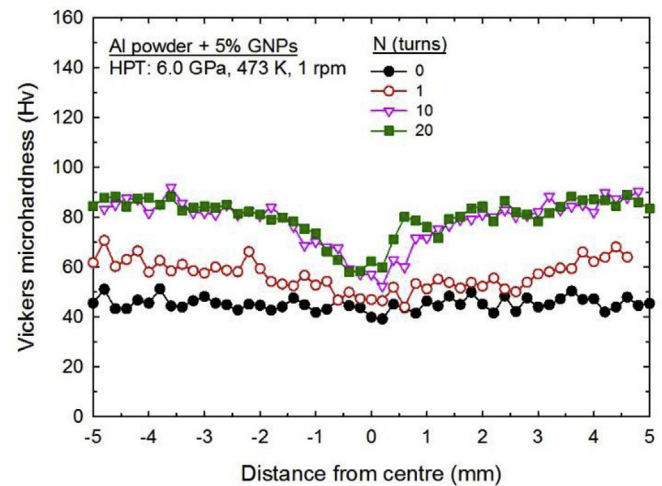
(c)

Fig. 11. Microhardness distributions along disc diameter in samples processed by HPT at (a) 298 K, (b) 373 K and (c) 473 K.
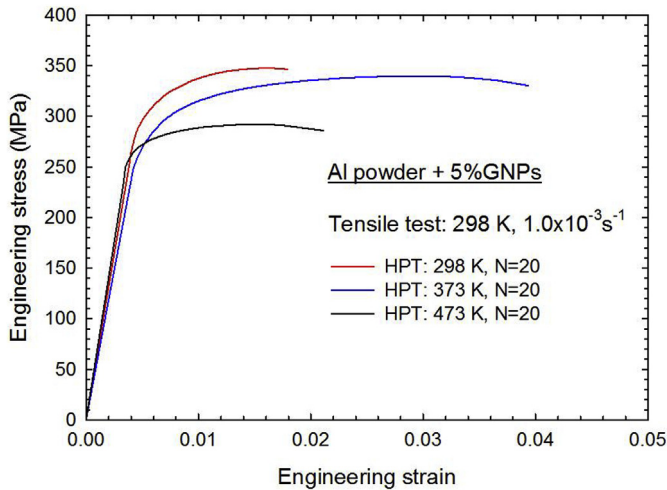
Fig. 12. Tensile results of 20 turns samples processed by HPT at different processing temperatures of 298, 373 and 473 K, and testing at 298 K.

particulates after heavy shear deformation [33,70] and the good homogeneity achieved in a nanocrystalline Cu-Cr alloy with an average grain size of less than 20 nm from an initial mixture of coarse Cu and Cr particles [71]. The successful processing of immiscible alloys by HPT also provides evidence of turbulent flow, mass transfer and the mixing of the deformed materials since a very high degree of chemical mixing was produced in the immiscible $Cu_{50}Ta_{50}$ system by the HPT deformation to high strains of stacks of Cu and Ta thin foils [51].

Based on these experimental observations and the simulations, it is reasonable to anticipate that the heavy shear strain applied by HPT will fragment the agglomerated GNPs in the Al matrix and redistribute the particles reasonably homogenously through the advent of turbulent flow. Figs. 2 and 3 confirms this trend for materials processed at 298 and 473 K, with a reduction in the extent of the GNPs agglomeration with increasing numbers of turns. This suggests that HPT may provide a powerful manufacturing route for obtaining uniform distributions of GNPs in an Al matrix through heavy shear deformation. This approach also overcomes the problem of the wettability between GNPs in an Al matrix which is an inherent feature of traditional liquid casting methods.

Furthermore, we noted that some graphene agglomerations remained even after high numbers of turns of HPT processing and this may limit any additional strength enhancement in the graphene-Al composites. Thus, the procedure for achieving a fully homogenous dispersion of graphene nanoplates in the Al matrix remains a challenge.

4.2. The effect of GNPs in improving the strength of HPT-processed graphene-Al nanocomposites

It was noted earlier that the composition of the Al powder is similar to that of the commercial purity (99.5%) Al-1050 alloy. Therefore, it is interesting to compare the strength of the HPT-processed graphene-Al nanocomposites with the Al-1050 alloy. After 5 turns of HPT at 298 K, the Al-1050 alloy shows a saturation hardness of ~65 Hv across the disc diameter [72,73] whereas in Fig. 11(a) the nanocomposite has not achieved saturation after 5 turns at 298 K with hardness values of ~40 Hv in the disc central area and ~90 Hv at the edge. There is also no saturation in the nanocomposite after 20 turns but with a maximum hardness of ~110 Hv from the disc half-radius to the edge. Thus, a much higher hardness is achieved at the edge of the nanocomposite which confirms the significant strengthening contribution from the GNPs.

It is well established that the equivalent von Mises strain, ε, imposed in HPT may be estimated from the relationship

$$\varepsilon = \frac{2\pi N r}{h\sqrt{3}} \tag{1}$$

where N is the number of HPT processing turns and r and h are the radius and height (or thickness) of the disc, respectively [62]. An early report demonstrated that all hardness datum points derived in HPT processing may be conveniently correlated by plotting against the equivalent strain [74]. Fig. 13 shows these plots for the nanocomposite at the three temperatures of (a) 298, (b) 373 and (c) 473 K. The saturation hardness at 298 K is ~110 Hv at equivalent strains above ~200, at 373 K the behaviour is similar to 298 K but with a saturation hardness of ~100 Hv at equivalent strains above ~200 and at 473 K there is a well-defined saturation at ~80 Hv at equivalent strains above ~50. These hardness distributions are similar to many other bulk metals except that the saturation then occurs at lower equivalent strains of ~30 in Al-1% Mg [75], ~50 in AZ31 alloy [76] and ~20 in tantalum [77]. This suggests the GNPs may interfere with dislocation slip in the Al matrix so that there is little or no recovery during the HPT processing.

Commercial purity Al-1050 sheet in an H14 state (work hardened by rolling) should have a tensile strength of ~105—145 MPa with a minimum of 12% elongation. Fig. 12 show that the graphene-Al nanocomposite has maximum strengths of ~350, ~340 and ~290 MPa after processing by HPT through 20 turns at 298, 373 and 473 K, respectively, and then testing in tension at 298 K. These values are therefore significantly higher than for the Al-1050 sheet. A comparison of grain refinement in the Al matrix when processing by HPT at 298 and 473 K is given in Fig. 14 and it is apparent that processing at 473 K produces a coarser grain structure with final grain sizes after 20 turns of ~70 and ~155 nm at 298 and 473 K, respectively. Thus, the HPT-processed graphene-Al nanocomposite has much higher strength than the commercial purity Al-1050 alloy but with limited ductility, where this strength enhancement may arise from the synergistic effect of grain size refinement, dislocation strengthening, GNPs reinforcement and stress transfer [78].

### 4.3. The nature of the graphene-Al interface after HPT processing

There is an *ab initio* simulation on the interaction between a graphene (0001) sheet and Al (111) layer in carbon-aluminium (C-Al) nanocomposite systems with a calculated cohesive energy of ~0.185 eV for the C-Al interface and an equilibrium separation distance of ~0.248 nm between the graphene and Al layers [79]. This calculated cohesive energy at the C-Al interface is much larger than the value of 0.0417 eV for the bulk C-Al system [80] and suggests that the interface bonding of the C-Al nanostructure is not simply a van der Waals type but rather it is metallic or semimetallic in nature [81]. The calculated equilibrium separation distance of 0.248 nm between the graphene (0001) layers and the Al (111) layers is smaller than the GNPs interlayer separation of 0.35 nm but larger than the Al (111) interplanar distance of 0.231 nm. In order to form coherent interfaces between the

Table 1
Electrical conductivity of HPT-processed graphene-Al composite at 298 and 473 K.
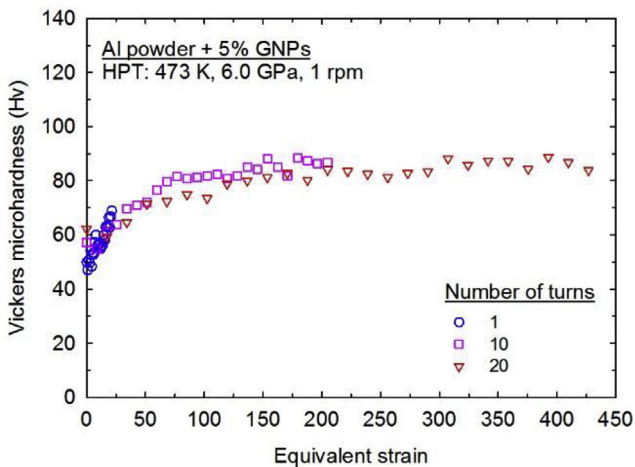
Sample condition	Electrical conductivity, IACS%
HPT processing at 298 K, N = 5	66.7 ± 4.0
HPT processing at 298 K, N = 20	64.9 ± 2.1
HPT processing at 473 K, N = 20	69.5 ± 2.3
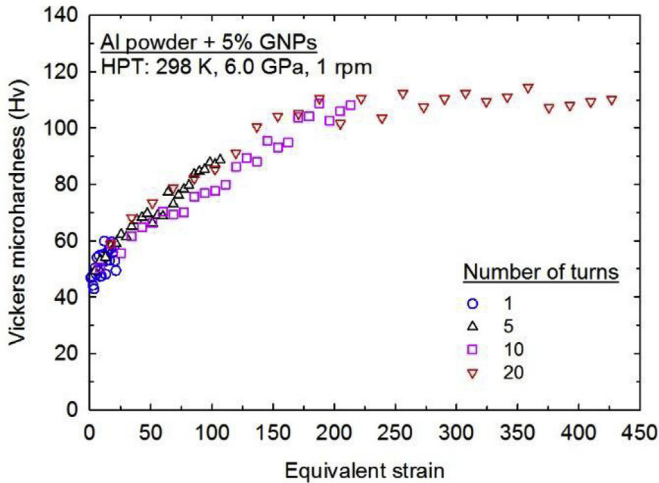
(a)
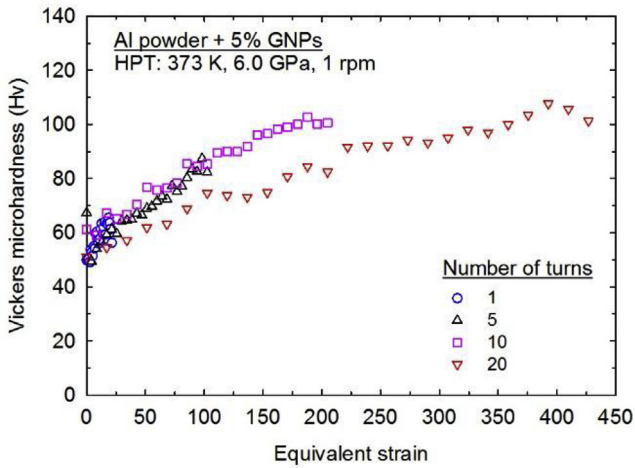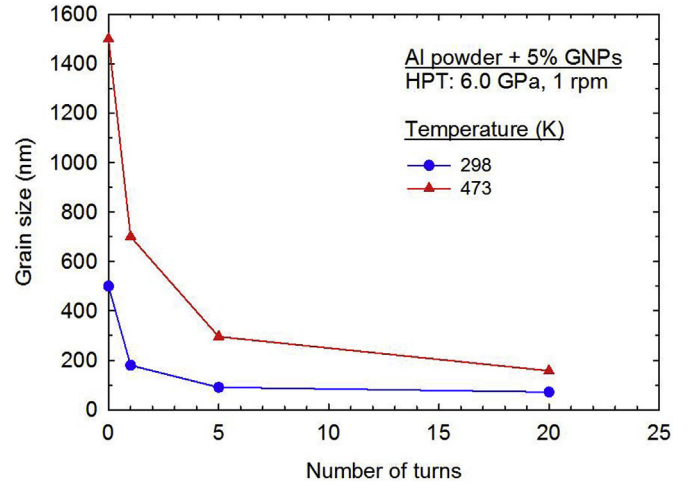
Fig. 14. Grain size comparison in graphene-Al composites processed at 298 and 473 K.

graphene (0001) sheets and the Al (111) planes, it is reasonable to assume that the interfacial spacing of the Al (111) layer near the interface is larger than the area without GNPs so that this interfacial area has a high dislocation density and microstrain within the Al lattice.

For a sample processed to 1 turn by HPT at 298 K as shown in Fig. 8(a), the graphene nanoplates have large orientation differences with the Al matrix (111) planes at lower numbers of turns which is consistent with the wide interfacial area. Due to the low shear strain induced at 1 turn of HPT, long straight and slightly curved GNPs are visible in the Al matrix in Fig. 8(b). At 473 K for 5 turns, the GNPs are dispersed and embedded within the grains, along the grain boundaries and in relatively large agglomerates in Fig. 9. The curvatures of the GNPs in Fig. 9 indicate heavy levels of local strain. Nevertheless, when the Al lattice (001) planes have the same orientation as the GNPs (0001) nanoplates, they merge together and it becomes difficult to clearly reveal the graphene nanoplates as in Fig. 9(b).

4.4. Factors affecting the electrical conductivity

The electrical conductivity is very sensitive to the microstructure of the metallic materials [81]. In practice, the electrical resistance of metals can be represented by Matthiessen's rule [59]:

$$\rho_{total} = \rho + \rho_{ss} + \rho_p + \rho_d + \rho_{gb} \tag{2}$$

where ρ_{total} is the total electrical resistance, ρ is the electrical resistivity of the lattice, ρ_{ss} is the resistivity due to solute atoms dissolved in the matrix, ρ_p is the resistivity added by second-phase precipitates, ρ_d is the resistivity due to dislocations present in the microstructure and ρ_{gb} is the resistivity due to grain boundaries.

The electrical conductivity of commercial purity Al in an annealed state with a coarse-grained structure is 62% IACS [82]. After HPT processing to 10 turns at 300 K, the electrical resistivity of commercial purity Al (99.5 wt%) was 30.5 nΩm [83], equivalent to 57.5% IACS. The drop of electrical conductivity in commercial purity Al arises from an electrical resistance increase due to the increased numbers of dislocations and grain boundaries ($\rho_d + \rho_{gb}$) after HPT processing.

In the fabricated graphene-Al nanocomposites, there is no significant effect from solute atoms (ρ_{ss}) and this term can be neglected. The GNPs as a reinforcement are different from second-phase precipitates and it is expected that the pi (π) electrons of

(b)

(c)

Fig. 13. Values of the Vickers microhardness plotted as a function of the equivalent strain for HPT-processed nanocomposites at (a) 298 K, (b) 373 K and (c) 473 K.

graphene will help to improve the conductivity. By contrast, the high dislocation densities and the significant grain refinement introduced by HPT processing increases the electrical resistance through ρ_d and ρ_{gb} and thereby reduces the electrical conductivity. This means the measured conductivity of the graphene-Al nano-composite will arise from these competing factors.

The electrical conductivities recorded in Table 1 show that in HPT processing at 298 K for 5 and 20 turns the average conductivities are higher than the reported conductivity of 57.5% IACS in commercial purity Al when processed to 10 turns by HPT at 300 K [83]. This suggests that the reinforcement by graphene produces a small improvement in the conductivity. There is also a further increase when the nanocomposite is processed by HPT at 473 K for 20 turns. In practice, HPT processing at 473 K may introduce some oxidation and this will increase the resistivity [84] but, in addition, processing at 473 K produces a lower dislocation density and a coarser grain structure when compared to HPT processing at 298 K as shown in Fig. 7 and this will effectively reduce the resistivity. Finally, it should be noted that, although the electrical conductivity is increased after processing by HPT at 473 K (Table 1), the tensile strength (Fig. 12) and the hardness (Fig. 13) are reduced at this processing temperature and this may limit the use of this material in practical applications.

5. Summary and conclusions

1. Graphene-Al nanocomposites with 5% GNPs reinforced in an Al matrix were successfully fabricated using HPT processing at 298, 373 and 473 K. Agglomerated GNPs were fragmented during HPT processing and tended to become more dispersed in the Al matrix as the numbers of turns increased.
2. Significant microstructural refinement was achieved in the Al matrix with average grain sizes of ~70 and ~155 nm after processing through 20 turns at 298 and 473 K, respectively.
3. The interface between graphene and the Al matrix showed long aligned graphene nanoplates at low numbers of turns and curved graphene plates after higher numbers of turns. The graphene nanoplates were present both within the Al grains and along the grain boundaries.
4. The HPT-processed graphene-Al nanocomposites have improved hardness and tensile strength by comparison with HPT-processed commercial purity Al. Therefore, the graphene reinforcement effectively improves the material strength.
5. These nanocomposites show a small improvement in conductivity compared with HPT-processed commercial purity Al at 298 K which suggests that graphene tends to improve the material conductivity.

Acknowledgements

References

[1] K.U. Kainer (Ed.), Metal Matrix Composites: Custom-made Materials for Automotive and Aerospace Engineering, Wiley-VCH, Weinheim, Germany, 2006.
[2] A.P. Mouritz (Ed.), Introduction to Aerospace Materials, Woodhead Publishing, Cambridge, U.K., 2012.
[3] Y. Huang, T.G. Langdon, The creep behaviour of discontinuously reinforced metal-matrix composites, JOM 55 (1) (2003) 15—20.
[4] E.P. Randviir, D.A.C. Brownson, C.E. Banks, A decade of graphene research: production, application and outlook, Mater. Today 17 (2014) 426—432.
[5] The Nobel Prize in Physics 2010, in: Graphene Compiled by the Class for Physics of Royal Swedish Academy of Sciences, The Nobel Foundation, Stockholm, Sweden, 5 October 2010.
[6] C. Lee, X. Wei, J.W. Kysar, J. Hone, Measurement of the elastic properties and intrinsic strength of monolayer graphene, Science 321 (2008) 385—388.
[7] A.A. Balandin, S. Ghosh, I. Bao, W. Calizo, D. Teweldebrhan, F. Miao, C. Lau, Superior thermal conductivity of single-layer graphene, Nano Lett. 8 (2008) 902—907.
[8] A.K. Geim, K.S. Novoselov, The rise of graphene, Nat. Mater. 6 (2007) 183—191.
[9] B. Li, W.H. Zhong, Review on polymer/graphite nanoplatelet nanocomposites, J. Mater. Sci. 46 (2011) 5595—5614.
[10] B.C. Kandpal, J. Kumar, H. Singh, Production technologies of metal matrix composite: a review, Int. J. Res. Mech. Eng. Technol. 4 (20) (2014) 27—32.
[11] N.H. Babu, S. Tzamtzis, B. Barekar, J.B. Patel, Z. Fan, Fabrication of metal matrix composites under intensive shearing, Solid State Phenom. 141—143 (2008) 373—378.
[12] I.A. Ibrahim, F.A. Mohamed, E.J. Lavernia, Particulate reinforced metal matrix composites — a review, J. Mater. Sci. 26 (1991) 1137—1156.
[13] R.S. Rana, R. Purohit, S. Das, Review of recent studies in Al matrix composites, Int. J. Sci. Eng. Res. 3 (6) (2012) 1—16.
[14] V. Viswanathan, T. Laha, K. Balani, A. Agarwal, S. Seal, Challenges and advances in nanocomposite processing techniques, Mater. Sci. Eng. R 54 (2006) 121—285.
[15] A. Feest, Materials and processing technology for PM MMCs, Met. Powder Rep. 47 (10) (1992) 40—45.
[16] M. Alipour, R. Eslami-Farsani, Synthesis and characterization of graphene nanoplatelets reinforced AA7068 matrix nanocomposites produced by liquid metallurgy route, Mater. Sci. Eng., A 706 (2017) 71, 28.
[17] H. Zhang, C. Xu, W. Xiao, K. Ameyama, C. Ma, Enhanced mechanical properties of Al5083 alloy with graphene nanoplates prepared by ball milling and hot extrusion, Mater. Sci. Eng., A 658 (2016) 8—15.
[18] J. Wang, Z. Li, G. Fan, H. Pan, Z. Chen, D. Zhang, Reinforcement with graphene nanosheets in aluminum matrix composites, Scripta Mater. 66 (2012) 594—597.
[19] P. Hidalgo-Manrique, S. Yan, F. Lin, Q. Hong, I.A. Kinloch, X. Chen, R.J. Young, X. Zhang, S. Dai, Microstructure and mechanical behaviour of aluminium matrix composites reinforced with graphene oxide and carbon nanotubes, J. Mater. Sci. 52 (2017) 13466—13477.
[20] G. Liu, B. Xiong, Effects of graphene content on microstructures and tensile property of graphene-nanosheets/aluminum composites, J. Alloy. Comp. 697 (2017) 31—36.
[21] S.J. Yan, S.L. Dai, X.Y. Zhang, C. Yang, Q.H. Hong, J.Z. Chen, Z.M. Lin, Investigating aluminium alloy reinforced by graphene nanoflakes, Mater. Sci. Eng., A 612 (2014) 440—444.
[22] X. Yang, T. Zou, C. Shi, E. Liu, C. He, Effect of carbon nanotube (CNT) content on the properties of in-situ synthesis CNT reinforced Al composites, Mater. Sci. Eng., A 660 (2016) 11—18.
[23] S.N. Alam, L. Kumar, Mechanical properties of aluminium based metal matrix composites reinforced with graphite nanoplatelets, Mater. Sci. Eng., A 667 (2016) 16—32.
[24] M. Rashad, F. Pan, Z. Yu, M. Asif, H. Lin, R. Pan, Investigation on microstructural, mechanical and electrochemical properties of aluminium composites reinforced with graphene nanoplatelets, Prog. Nat. Sci.: Met. Mater. Int. 25 (2015) 460—470.
[25] B. Chen, K. Kondoh, H. Imai, J. Umeda, M. Takahashi, Simultaneous enhancing strength and ductility of carbon nanotube/aluminium composites by improving bonding condition, Scripta Mater. 113 (2016) 158—162.
[26] A. Bhadauria, L.K. Singh, T. Laha, Effect of physio-chemically functionalized graphene nanoplatelet reinforcement on tensile properties of aluminum nanocomposite synthesized via spark plasma sintering, J. Alloy. Comp. 748 (2018) 783—793.
[27] A. Bisht, M. Srivastava, R.M. Kumar, I. Lahiri, D. Lahiri, Strengthening mechanism in graphene nanoplatelets reinforced aluminium composite fabricated through spark plasma sintering, Mater. Sci. Eng., A 695 (2017) 20—28.
[28] R. Rajeshkumar, V. Udhayabanu, A. Srinivasan, K.R. Ravi, Microstructural evolution in ultrafine grained Al-graphite composite synthesized via combined use of ultrasonic treatment and friction stir processing, J. Alloy. Comp. 726 (2017) 358—366.
[29] R.A. Rapp, X. Zheng, Thermodynamic consideration of grain refinement of aluminum alloys by titanium and carbon, Metall. Trans. A 22A (1991) 3071—3075.
[30] Y. Huang, T.G. Langdon, Advances in ultrafine-grained materials, Mater. Today 16 (3) (2013) 85—92.
[31] A. Bachmaier, R. Pippan, New procedure to generate stable nanocrystallites by severe plastic deformation, Intl Mater. Res. 58 (2013) 41—62.
[32] M. Khajouei-Nezhad, M.H. Paydar, R. Ebrahimi, P. Jenei, P. Nagy, J. Gubicza, Microstructure and mechanical properties of ultrafine-grained aluminum consolidated by high-pressure torsion, Mater. Sci. Eng., A 682 (2017) 501—508.
[33] A. Bachmaier, A. Hohenwarter, R. Pippan, New procedure to generate stable nanocrystallites by severe plastic deformation, Scripta Mater. 61 (2009) 1016—1019.
[34] R.Z. Valiev, R.S. Mishra, J. Groza, A.K. Mukherjee, Processing of nanostructured

nickel by severe plastic deformation consolidation of ball-milled powder, Scripta Mater. 34 (1996) 1443–1448.

[35] K. Edalati, Z. Horita, H. Fujiwara, K. Ameyama, Cold consolidation of ball-milled *titanium powders* using high-pressure torsion, Metall. Mater. Trans. 41A (2010) 3308–3317.

[36] A.P. Zhilyaev, G. Ringot, Y. Huang, J.M. Cabrera, T.G. Langdon, Mechanical behavior and microstructure properties of titanium powder consolidated by high-pressure torsion, Mater. Sci. Eng., A 688 (2017) 498–504.

[37] E. Menendez, G. Salazar-Alvarez, A.P. Zhilyaev, S. Surinach, M.D. Baro, J. Nogues, J. Sort, Cold Consolidation of metal-ceramic nanocomposite powders with large ceramic fractions, Adv. Funct. Mater. 18 (2008) 3293–3298.

[38] I. Sabirov, O. Kolednik, R. Pippan, Homogenization of metal matrix composites by high-pressure torsion, Metall. Mater. Trans. 36A (2005) 2861–2870.

[39] R.K. Islamgaliev, W. Buchgraber, Y.R. Kolobov, N.M. Amirkhanov, A.V. Sergueeva, K.V. Ivanov, G.P. Grabovetskaya, Deformation behavior of Cu-based nanocomposite processed by severe plastic deformation, Mater. Sci. Eng., A 319–321 (2001) 872–876.

[40] I.V. Alexandrov, Y.T. Zhu, T.C. Lowe, R.K. Islamgaliev, R.Z. Valiev, Consolidation of nanometer sized powders using severe plastic torsional straining, Nanostruct. Mater. 10 (1998) 45–54.

[41] T. Tokunaga, K. Kaneko, K. Sato, Z. Horita, Microstructure and mechanical properties of aluminum-fullerene composite fabricated by high pressure torsion, Scripta Mater. 58 (2008) 735–738.

[42] T. Tokunaga, K. Kaneko, Z. Horita, Production of aluminium-matrix carbon nanotube composite using high pressure torsion, Mater. Sci. Eng., A 490 (2008) 300–304.

[43] H. Asgharzadeh, S.-Y. Joo, H.S. Kim, Al/C60 nanocomposites fabricated by high-pressure torsion, Metall. Mater. Trans. 46A (2015) 1838–1842.

[44] S.H. Joo, S.C. Yoon, C.S. Lee, D.H. Nam, S.H. Hong, H.S. Kim, Microstructure and tensile behaviour of Al and Al-matrix carbon nanotube composites processed by high pressure torsion of the powders, J. Mater. Sci. 45 (2010) 4652–4658.

[45] M.R. Akbarpour, M. Farvizi, D.J. Lee, H. Rezaei, H.S. Kim, Effect of high-pressure torsion on the microstructure and strengthening mechanism of hot-consolidated Cu-CNT nanocomposite, Mater. Sci. Eng., A 638 (2015) 289–295.

[46] P. Jenei, J. Gubicza, E.Y. Yoon, H.S. Kim, J.L. Lábár, High temperature thermal stability of pure copper and copper-carbon nanotube composites consolidated by high pressure torsion, Composites Part A 51 (2013) 71–79.

[47] P. Jenei, E.Y. Yoon, J. Gubicza, H.S. Kim, J.L. Lábár, T. Ungár, Microstructure and hardness of copper-carbon nanotube composites consolidated by high pressure torsion, Mater. Sci. Eng., A 528 (2011) 4690–4695.

[48] H. Li, A. Misra, Y. Zhu, Z. Horita, C.C. Koch, T.G. Holesinger, Processing and characterization of nanostructured Cu-carbon nanotube composites, Mater. Sci. Eng., A 523 (2009) 60–64.

[49] R. Kulagin, Y. Beygelzimer, Y. Ivanisenko, A. Mazilkin, H. Hahn, High pressure torsion: from laminar flow to turbulence, IOP Conf. Ser. Mater. Sci. Eng. 194 (1–6) (2017), 012045.

[50] K. Edalati, H. Emami, Y. Ikeda, H. Iwaoka, I. Tanaka, E. Akiba, Z. Horita, New nanostructured phases with reversible hydrogen storage capability in immiscible magnesium-zirconium system produced by high-pressure torsion, Acta Mater. 108 (2016) 293–303.

[51] N. Ibrahim, M. Peterlechner, F. Emeis, M. Wegner, S.V. Divinski, G. Wilde, Mechanical alloying via high-pressure torsion of the immiscible Cu$_{50}$Ta$_{50}$ system, Mater. Sci. Eng., A 685 (2017) 19–30.

[52] R.B. Figueiredo, P.R. Cetlin, T.G. Langdon, Using finite element modeling to examine the flow processes in quasi-constrained high-pressure torsion, Mater Sci Eng A 528 (2011) 8198–8204.

[53] G.E. Dieter, Mechanical Metallurgy, McGraw-Hill, New York, NY, USA, 1988, p. 304.

[54] R.B. Figueiredo, S. Sabbaghianrad, A. Giwa, J.R. Greer, T.G. Langdon, Evidence for exceptional low temperature ductility in polycrystalline magnesium processed by severe plastic deformation, Acta Mater. 122 (2017) 322–331.

[55] Copper Wire Tables (Technical report), Circular of the Bureau of Standards No.31, 3d ed., United States Department of Commerce, Washington DC, October 1914.

[56] A.C. Ferrari, J.C. Meyer, V. Scardaci, C. Casiraghi, M. Lazzeri, F. Mauri, S. Piscanec, D. Jiang, K.S. Novoselov, S. North, A.K. Gem, Raman spectrum of graphene and graphene layers, Phys. Rev. Lett. 97 (2006), 187401-18704.

[57] C. He, N. Zhao, C. Shi, X. Du, J. Li, H. Li, Q. Cui, An approach to obtaining homogeneously dispersed carbon nanotubes in Al powders for preparing reinforced Al-matrix composites, Adv. Mater. 19 (2007) 1128–1132.

[58] M. Kawasaki, Different models of hardness evolution in ultrafine-grained materials processed by high-pressure torsion, J. Mater. Sci. 49 (2014) 18–34.

[59] P.L. Rossiter, The Electrical Resistivity of Metals and Alloys, Cambridge University Press, Cambridge, U.K., 2003.

[60] R.K. Islamgaliev, K.M. Nesterov, Y. Champion, R.Z. Valiev, Enhanced strength and electrical conductivity in ultrafine-grained Cu-Cr alloy processed by severe plastic deformation, IOP Conf. Ser. Mater. Sci. Eng. 63 (1–6) (2014), 012118.

[61] S.V. Dobatkin, J. Gubicza, D.V. Shangina, N.R. Bochvar, N.Y. Tabachkova, High strength and good electrical conductivity in Cu-Cr alloys processed by severe plastic deformation, Mater. Lett. 153 (2015) 5–9.

[62] R.Z. Valiev, YuV. Ivanisenko, E.F. Rauch, B. Baudelet, Structure and deformation behaviour of Armco iron subjected to severe plastic deformation, Acta Mater. 44 (1996) 4705–4712.

[63] Y. Cao, Y.B. Wang, S.N. Alhajeri, X.Z. Liao, W.L. Zheng, S.P. Ringer, Y.T. Zhu, A visualization of shear strain in processing by high-pressure torsion, J. Mater. Sci. 45 (2010) 765–770.

[64] Y. Cao, M. Kawasaki, Y.B. Wang, S.N. Alhajeri, X.Z. Liao, W.L. Zheng, S.P. Ringer, Y.T. Zhu, T.G. Langdon, Unusual macroscopic shearing patterns observed in metals processed by high-pressure torsion, J. Mater. Sci. 45 (2010) 4545–4553.

[65] Y. Cao, Y.B. Wang, R.B. Figueiredo, L. Chang, X.Z. Liao, M. Kawasaki, W.L. Zheng, S.P. Ringer, T.G. Langdon, Y.T. Zhu, Three-dimensional shear-strain patterns induced by high-pressure torsion and their impact on hardness evolution, Acta Mater. 59 (2011) 3903–3914.

[66] Y. Huang, M. Kawasaki, T.G. Langdon, Influence of anvil alignment on shearing patterns in high-pressure torsion, Adv. Eng. Mater. 15 (2013) 747, 655.

[67] Y. Huang, M. Kawasaki, T.G. Langdon, An investigation of flow pattern and hardness distribution using different anvil alignments in high-pressure torsion, J. Mater. Sci. 48 (2013) 4533–4542.

[68] Y.Z. Tian, X.H. An, S.D. Wu, Z.F. Zhang, R.B. Figueiredo, N. Gao, T.G. Langdon, Direct observations of microstructural evolution in a two-phase Cu-Ag alloy processed by high-pressure torsion, Scripta Mater. 63 (2010) 65–68.

[69] M. Pouryazdan, B.J.P. Kaus, A. Rack, A. Ershov, H. Hahn, Mixing instabilities during shearing of metals, Nat. Commun. 8 (1–7) (2017) 1611.

[70] I. Sabirov, O. Kolednik, R.Z. Valiev, R. Pippan, Equal channel angular pressing of metal matrix composites: effect on particle distribution and fracture toughness, Acta Mater. 53 (2005) 4919–4930.

[71] J. Guo, J.M. Rosalie, R. Pippan, Z. Zhang, Revealing the microstructural evolution in Cu-Cr nanocrystalline alloys during high pressure torsion, Mater. Sci. Eng., A 695 (2017) 350–359.

[72] S.N. Alhajeri, M. Kawasaki, N. Gao, T.G. Langdon, The evolution of homogeneity during processing of aluminium alloys by HPT, Mater. Sci. Forum 667–669 (2011) 277–282.

[73] M. Kawasaki, S.N. Alhajeri, C. Xu, T.G. Langdon, The development of hardness homogeneity in pure aluminum and aluminum alloy disks processed by high-pressure torsion, Mater. Sci. Eng., A 529 (2011) 345, 251.

[74] A. Vorhauer, R. Pippan, On the homogeneity of deformation by high pressure torsion, Scripta Mater. 51 (2004) 921–925.

[75] O. Andreau, J. Gubicza, N.X. Zhang, Y. Huang, P. Jenei, T.G. Langdon, Effect of short-term annealing on the microstructures and flow properties of an Al-1% Mg alloy processed by high-pressure torsion, Mater. Sci. Eng., A 615 (2014) 231–239.

[76] Y. Huang, R.B. Figueiredo, T. Baudin, F. Brisset, T.G. Langdon, Evolution of strength and homogenity in a magnesium AZ31 alloy processed by high-pressure torsion at different temperatures, Adv. Eng. Mater. 14 (2012) 1018–1026.

[77] N. Maury, N.X. Zhang, Y. Huang, A.P. Zhilyaev, T.G. Langdon, A critical examination of pure tantalum processed by high-pressure torsion, Mater. Sci. Eng., A 638 (2015) 174–182.

[78] J. Wang, Z. Li, G. Fan, H. Pan, Z. Chen, D. Zhang, Reinforcement with graphene nanosheets in aluminium matrix composites, Scripta Mater. 66 (2012) 594–597.

[79] W. Lee, S. Jang, M.J. Kim, J.-M. Myoung, Interfacial interactions and dispersion relations in carbon-aluminium nanocomposite systems, Nanotechnology 19 (1–13) (2008) 285701.

[80] Y. Qiu, L.G. Hector, N. Ooi, J.B. Adams, A first principles study of adhesion and adhesive transfer at Al (111)/graphite (0001), Surf. Sci. 581 (2005) 155–168.

[81] R.Z. Valiev, M.Yu Murashkin, I. Sabirov, A nanostructureal design to produce high-strength Al alloys with enhanced electrical conductivity, Scripta Mater. 76 (2014) 13–16.

[82] E.V. Bobruk, M.Yu Murashkin, V.U. Kazykhanov, R.Z. Valiev, Aging behavior and properties of ultrafine-grained aluminum alloys of Al-Mg-Si system, Rev. Adv. Mater. Sci. 31 (2012) 109–115.

[83] A.M. Mavlyutov, A.S. Bondarenko, M.Yu Murashkin, E.V. Boltynjuk, R.Z. Valiev, T.S. Orlova, Effect of annealing on microhardness and electrical resistivity of nanostructured SPD aluminium, J. Alloy. Comp. 698 (2017) 539–546.

[84] Y. Miyajima, S.-Y. Komatsu, M. Mitsuhara, S. Hata, H. Nakashima, N. Tsuji, Change in electrical resistivity of commercial purity aluminium severely plastic deformed, Phil. Mag. 90 (2010) 4475–4488.